Ocean Engineering 259 (2022) 111890

Contents lists available at ScienceDirect

Ocean Engineering

journal homepage: www.elsevier.com/locate/oceaneng

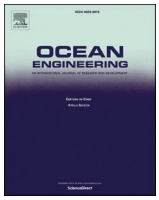

# Research on risk assessment method of steel catenary riser based on information fusion

Peijie Yang [a], Lusheng Jia [b], Zhuang Kang [a], Jichuan Kang [a,c,*]

[a] College of Shipbuilding Engineering, Harbin Engineering University, Harbin, China
[b] Subsea Pipeline Section, Engineering R&D Dept. CNOOC Research Institute, CNOOC, Beijing, China
[c] HEU-UL International Joint Laboratory of Naval Architecture and Offshore Technology, Harbin, 150001, China

ARTICLE INFO

*Keywords:*
Steel catenary riser
Information fusion
Risk assessment
Desert-Smarandache theory

ABSTRACT

The Steel Catenary Riser (SCR) is an essential component connecting the subsea production system and the offshore floating platform and SCR malfunction leads to disastrous consequences. In order to ensure operation safety, the operating company monitors SCR motion response in real time by installing sensors. This paper aims to develop a multi-sensor information fusion algorithm for SCR risk assessment. The algorithm generates basic probability assignment (BPA) function based on known information. Then, the intuitionistic fuzzy multi-attribute decision matrix is constructed by BPA to evaluate the dynamic reliability of the sensor. Finally, the focal element credibility is calculated to reduce the conflict between evidences, and the improved Desert-Smarandache (DSm) theory fusion rule is utilized to evaluate the SCR risk through decision fusion. The feasibility of this method is verified by the case study. The corresponding risk control strategy is also provided.

## 1. Introduction

As a transmission pipeline connecting underwater oil production system and offshore floating platform device, marine riser is one of the most important components of floating oil and gas development system. Marine risers have many types, among which SCR (Yuan et al., 2021; Cheng et al., 2020) is widely applied in deep-water oil and gas development due to its economy and practicability. The working environment of SCR is time-varying and to a large extent uncertain. Even if measures such as improving the safety factor and design standard are taken to improve the structural strength of the riser in the design phase, the SCR may still have fracture damage, such as fatigue fracture failure, buckling failure and overload fracture failure. In terms of the offshore structures, high maintenance or replacement costs are required (Li et al., 2021). Therefore, it is an essential step to ensure the durability and safety of structures during their life cycle is a crucial step (Ni et al., 2022).

During the service of the SCR, the forces are extremely complex. The top of the riser, which is subjected to kinematic loads, comes from the upper floating platform. The interior is subjected to high temperatures and pressure loads. Externally it is subjected to dynamic loads from waves and currents as well as the resistance effects of the subsea soil. Of which, the upper floating platform is subject to environmental factors such as wind, waves and currents (Li et al., 2022), and the constant cyclic movement around the top of the riser leads to fatigue fracture damage in the area where the top of the SCR is connected to the upper floating platform. In the touchdown zone, the cyclic movement of the pipe and the non-linear nature of the soil lead to fatigue fracture damage at the touchdown point of the riser (Nakhaee et al., 2010; Yuan et al., 2017), as well as the phenomenon of vortex-induced vibration (VIV) of the riser under the influence of waves and currents, causing fatigue fracture at the riser touchdown point (Wang et al., 2015). In order to ensure the safe service of the SCR during its life cycle, it is necessary to conduct a detailed study and research of the causes and performance modes of SCR failure.

Substantial experimental and theoretical researches have been put into increasing the understanding of the failure mechanism and failure mode of SCR. Elosta (2013), Gao et al. (2017), Fu and Yang (2010) To describe the complexity of SCR-soil interaction, mathematical modeling plays a central role. This includes the model of SCR breaking through soil resistance under random waves, the P–Y curve model considering tube-soil separation and including soil suction effects, and the SCR fatigue model under the SN method. Initially, experimental studies were mainly interested in the fatigue of SCR touchdown point under fluid action. Although VIV is known to cause SCR vibration, this vibration is

* Corresponding author. College of Shipbuilding Engineering, Harbin Engineering University, Harbin, China.
*E-mail address:* kangjichuan@hrbeu.edu.cn (J. Kang).

https://doi.org/10.1016/j.oceaneng.2022.111890
Received 7 March 2022; Received in revised form 29 May 2022; Accepted 2 July 2022
Available online 11 July 2022

minor in magnitude and is considered to have a negligible effect on riser fatigue. However, Wang et al. (2013) proposed that cross-flow (CF) VIV of SCR near the touchdown point causes fatigue damage and validated the proposed model. Komachi and Mazaheri (2018) and Thorsen et al. (2015) investigated the three-dimensional response of riser under VIV with fatigue damage by simulating the relationship. The contribution of inline cross-flow VIV to fatigue damage is significant and should not be neglected. To this purpose, Zheng (2014) constructed a database of inline cross-flow VIV hydrodynamic coefficients and systematically analyzed several key hydrodynamic coefficients in the database. Xue et al. (2014) proposed a fatigue damage prediction model for riser considering cross-flow and online vibration, and verified the validity of the method. Another recent experiment showed that the suspension zone and touchdown zone are most susceptible to fatigue damage (Ebunuoha et al., 2017).

With the improved understanding of damage and failure of offshore riser, risk assessment techniques for riser have also advanced significantly. In the mid-1970s, quantitative risk assessment (QRA) method was mainly used to assess the risk of offshore platform system. In 1990, the British Offshore Oil Industry Association put forward a comprehensive risk assessment method and a safety case specification in 1992. In 1993, the Norwegian Petroleum Commission issued a new NORSOK code to achieve unified risk assessment and management of offshore structures. In 2000, DET NORSKE VERITAS (2001) issued relevant regulations on risk assessment for offshore riser and pipeline protection. The standard specifies the quantitative risk assessment system for new pipelines. In addition to the technical specifications for risk assessment of marine risers formulated by the classification society, researchers have also conducted valuable research. Alzbutas et al. (2014) implemented risk assessment of risers based on historical failure data of risers, modeled according to a Bayesian approach. Nazir et al. (2008) implemented a Monte Carlo approach, and the deep-water rigid marine risers associated with Morison wave loads were reliability was analyzed. Abhulimen (2009) proposed a risk assessment model for the FPSO-riser system using Monte Carlo and Markov chain algorithms. The reliability analysis of the riser internal wave corrosion, which was carried out by Hu et al. (2014) using a first-order reliability numerical evaluation method, and the results were validated by Monte Carlo significant sampling. The reliability of the composite conduit riser was analyzed and optimized by Shen et al. (2014) using Monte Carlo method. Khan and Ahmad (2007) performed the risk analysis of the riser by using the modified AFOSM and Monte Carlo method.

These valuable studies have greatly contributed to the development of risk assessment techniques for marine risers. At present, as SCR become the mainstream of oil and gas deep-sea development riser systems, the complex and changing marine environment has posed a great challenge to the long-term service safety of SCR. For this specific reason, the marine riser monitoring technology was created. This technology is to install sensors in the parts of the riser that are subjected to large alternating loads as well as in the bending and contact areas, and to predict and alarm sudden disasters through the data monitored in real time. The SCR on which the monitoring system was installed was first applied on the P-18 semi-submersible platform in Brazil in 1998. The whole monitoring system includes meteorological sensors, marine meteorological floats, acceleration sensors, strain sensors and inclination sensors and other environmental monitoring equipment. Among them, part of the riser monitoring equipment is shown in Fig. 1.

The failure factors of SCR are somewhat random and ambiguous. The measurement of the potential failure risk of SCR in traditional risk assessment is inadequate, and therefore the safety of SCR throughout their life cycle is inconvenient to assess accurately. In recent years, information fusion-based methods have been rapidly developed in the fields of target identification, medical diagnosis, risk assessment, and mechanical fault diagnosis, as Zhou et al. (2020) proposed a new method that coupled the risk management system and a quality management system, and performed information fusion of monitoring data, design data, and environmental data with DS evidence theory, as well as risk assessment of the shield cutter accident of Xiamen Metro Line 3. Masoumi et al. (2019) evaluated the risk and determined the risk level of each team building utilizing information fusion techniques with the spatial information generated by drones on buildings. It is natural for us to consider the usage of information fusion techniques for risk assessment of SCR. Therefore, in order to provide a dynamic and reliable risk assessment tool, this study proposes an information fusion-based SCR risk assessment method. Compared with other methods of risk assessment, the proposed method in this paper does not require a large amount of a priori information of failure. It fuses information from the motion response information obtained from real-time monitoring of multiple sensors on the riser, so as to obtain an accurate estimation of the riser risk state. The proposed method also combines the advantages of intuitionistic fuzzy set theory and evidence theory and is applied to reduce the ambiguity and uncertainty existing in SCR risk assessment, and it also fulfills the requirements of risk assessment under single-failure or multi-coupling failure scenarios in SCR. In this paper, a deep-water semi-submersible oil and gas development system under the action of tropical cyclones in the South China Sea is illustrated. First, the overall intensity of SCR under the action of a strong typhoon is analyzed in OrcaFlex, and then a multi-source information fusion model is established. Finally, the information fusion model is used to assess the risk of SCR.

The rest of the paper is organized as follows. In Section 2, we present the Intuitionistic fuzzy set theory and the Desert-Smarandache theory (Vladareanu et al., 2015). The information fusion algorithm based on intuitionistic fuzzy evidence proposed in this paper is described in Section 3. Section 4 illustrates the application of information fusion in SCR risk assessment. Finally, an abbreviated conclusion is offered in

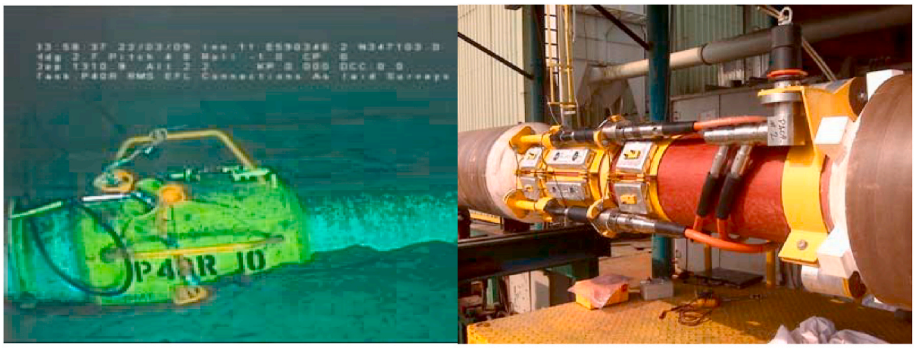

(a) Touchdown zone strain monitoring unit (b) Suspension zone strain monitoring unit

**Fig. 1.** Fig. 1. Schematic diagram of SCR partial monitoring system equipment.

Section 5.

## 2. Risk assessment technology

### 2.1. Intuitionistic fuzzy set theory

In the risk assessment of SCR, ambiguity is prevalent in describing the risk since the failure mechanism has not been fully clarified. Fuzzy set theory (Guo et al., 2021) deals with this fuzzy information by generating an affiliation function, but to be closer to the fuzzy reasoning process of human thought patterns, the intuitive fuzzy set theory (IFS) (Garg and Rani, 2020; Zhang and Zhu, 2021; Tao et al., 2021; Yazdi, 2018) proposed by Bulgarian scholar Atanassov was developed in 1986. Compared with the concept of membership degree in fuzzy set theory, intuitionistic fuzzy sets add non-membership degree to describe uncertainty in a more elaborate way. Therefore, this paper chooses to apply intuitionistic fuzzy set theory to deal with the fuzzy information in the risk assessment of SCR.

In the intuitionistic fuzzy set, let $X = \{x_1, x_2, \cdots, x_n\}$ be a non-empty theoretical domain, the intuitionistic fuzzy set ax on Definition $A = \{\langle x, \mu_A(x), \upsilon_A(x)\rangle | x \in X\}$

where $\mu_A(x)\ X \rightarrow [0,1]$ and$\upsilon_A(x)\ X \rightarrow [0,1]$ correspondingly define the degree to which an element $x$ in $X$ definitely belongs to a subset $A$ of $X$ and definitely does not belong to $A$. Apparently, the subordination of the intuitionistic fuzzy set $A$ is restricted to the subset $[\mu_A(x), 1-\upsilon_A(x)]$ of [0,1]. $\mu_A(x)$ is called the subordination function of $x$ to $A$ and $\upsilon_A(x)$ is called the unaffiliation function of $x$ to $A$. For any $\forall x \in X, 0 \leq \mu_A(x) + \upsilon_A(x) \leq 1$.

Since the sum of the affiliation function and the non-affiliation function is not greater than 1, another function can be derived, that is the hesitation function. Called $\pi_A(x)\ X \rightarrow [0,1]$ as the hesitation function of$x$ relative to$A$, the hesitation function $\pi_A(x)$ is denoted as: $\pi_A(x) = 1 - \mu_A(x) - \upsilon_A(x)$.

The hesitancy function $\pi_A(x)$ represents a measure of the hesitation of an element $x$ belonging to$A$ and $\forall x \in X, \pi_A(x) \in [0,1]$.

Let the whole set of intuitionistic fuzzy sets on the theoretical domain $X$ be $IFS_S(X)$, and $\forall A \in IFS_S(X)$.

### 2.2. Desert-Smarandache theory

DS evidence theory (Gong et al., 2018; Yang et al., 2021; Khakzad, 2019; Misuri et al., 2019) was evolved during the 1970s by the combined effort of Dempster and Shafer (DS). DS Evidence theory uses three basic parameters, i.e., basic probability assignment (BPA), belief measure (Bel), and plausibility measure (Pl) to characterize the un-certainty in a belief structure. The belief structure represents a continuous interval [belief, plausibility] in which true probability may lie.

However, all elements in DS evidence theory are exclusive, that is, propositions are independent of each other. In practical application, the boundary of each proposition is fuzzy and there may be intersection. Taking fault diagnosis as an example, there may be multiple coupling faults, which cannot be solved by the exclusivity of DS evidence theory. Therefore, Desert, Smarandache and other scholars jointly developed a new plausible and paradoxical reasoning theory in 2002, also known as Desert Smarandache theory (Dezert, 2002; Smarandache and Dezert, 2013; Yi et al., 2013; Vatsa et al., 2009a,b), which is referred to as DSm theory for short. DSm theory is an extension of the traditional DS evidence theory, which can effectively deal with the sources of evidence from uncertainty, inaccuracy and high inconsistency. It solves the problem that concurrent faults cannot be represented in the framework of DS evidence theory to a great extent.

The generalized identification framework $\Theta = \{\theta_1\ \theta_2\ \ldots\ \theta_n\}$ is a finite nonempty universe, which is composed of n complete assumptions. The set generated by cross merging the elements in $\Theta$ is called super power set $D^\Theta$. If the mapping $m : D^\Theta \rightarrow [0,1]$ meets the following conditions:

The generalized identification framework $\Theta = \{\theta_1\ \theta_2\ \ldots\ \theta_n\}$ is a finite nonempty universe,

$$\begin{cases} m(\varnothing) = 0 \\ m(A) > 0 \\ \sum\limits_{A \in D^\Theta} m(A) = 1 \end{cases} \tag{1}$$

Among them, $m$ is called generalized basic probability assignment.

Analogous to the trust quantization function in DS evidence theory, DSm theory also defines generalized confidence function and generalized plausibility function on super power set $D^\Theta$. They are expressed by equations (2) and (3) respectively.

$$Bel(A) = \sum_{B \subseteq A, B \in D^\Theta} m(B) \tag{2}$$

$$Pl(A) = \sum_{B \cap A \neq \varnothing, B \in D^\Theta} m(B) \tag{3}$$

Since DSm theory is an extension of DS evidence theory, which resembles the Dempster combination rule in DS evidence theory, there are two combination rules in DSm theory: the free DSm model and the hybrid DSm model (Vatsa et al., 2009a,b):

For the free DSm model, it is assumed that on the identification framework $\Theta$, $A$ and $B$ are two independent evidences, and their generalized basic probability functions are $m_1$ and $m_2$ respectively. When acting at the same time, for a given $C \in D^\Theta$, the synthesis formula is as follows:

$$m(C) = \sum_{\substack{A,B \in D^\Theta \\ A \cap B = C}} m_1(A) m_2(B) \tag{4}$$

For the hybrid DSm model, it is assumed that n evidences on the identification framework $\Theta$ are independent of each other, and their BPAS are $m_1, m_2, \cdots, m_k$, When acting simultaneously, for a given $A \in D^\Theta$, the synthesis formula is as follows:

$$m(A) = \delta(A)[S_1(A) + S_2(A) + S_3(A)] \tag{5}$$

All sets contained in the expression are in canonical form, where $\delta(A)$ is the characteristic non empty function of set $A$. if $A \notin D^\Theta$, $\delta(A) = 1$, otherwise $\delta(A) = 0$. Here is $\varnothing = \{\varnothing_t, \varnothing\}$, $\varnothing$ is an empty set in the classical or ordinary meaning, and $\varnothing_t$ is the set of elements forced to be empty in the super power set $D^\Theta$, which is constrained by the hybrid DSm model.

$S_1(A)$ (Free DSm model), $S_2(A)$, $S_3(A)$ defined as follows:

$$\begin{aligned} S_1(A) &= \sum_{\substack{X_1, X_2, \cdots, X_k \in D^\Theta \\ X_1 \cap X_2 \cap \cdots \cap X_k = A}} \prod_{i=1}^{k} m_i(X_i) \\ S_2(A) &= \sum_{\substack{X_1, X_2, \cdots, X_k \in \varnothing \\ [u=A] \vee [(u \in \varnothing) \wedge (A = I_t)]}} \prod_{i=1}^{k} m_i(X_i) \\ S_3(A) &= \sum_{\substack{X_1, X_2, \cdots, X_k \in D^\Theta \\ X_1 \cup X_2 \cup \cdots \cup X_k = A \\ X_1 \cap X_2 \cap \cdots \cap X_k \in \varnothing}} \prod_{i=1}^{k} m_i(X_i) \end{aligned} \tag{6}$$

where $u = u(X_1) \cup u(X_2) \cup \cdots \cup u(X_k)$ and $u(X)$ contains the union $X$ of all components $\theta_i$, and $I_t = \theta_1 \cup \theta_2 \cup \cdots \cup \theta_n$ represents complete unknown. $S_1(A)$ represents the combination of $k$ independent information sources under the free DSm model; $S_2(A)$ represents the relative or complete unknown quantity that transforms BPA of all relative and

absolute empty sets; $S_3(A)$ represents the union of non-empty sets converted by GBPA of relatively empty sets. $S_2(A)$ and $S_3(A)$ represent faults that cannot occur in actual fault diagnosis (including concurrent faults), or faults that disappear after repair. After redefining these faults as $\varnothing$, the information contained in these faults will be redistributed to prevent the loss of useful information.

## 3. Information fusion algorithm based on intuitionistic fuzzy evidence

The proposed SCR risk assessment framework is presented in Fig. 2. There are three basic steps, namely, construction of BPA, dynamic reliability evaluation, evidence conflict resolution and decision fusion algorithm. Step1: the BPA construction does not require a large amount of a priori information of riser failure, which can be obtained by the computational processing of real-time monitoring data; step2: the dynamic reliability assessment of sensors is accomplished by utilizing the intuitionistic fuzzy multi-attribute decision matrix to deal with the uncertain information existing in various sensors monitoring data; step3: the final decision fusion is carried out by considering the possible single-failure or multi-coupling failure scenarios of SCR. The following sections will explain the algorithm in detail.

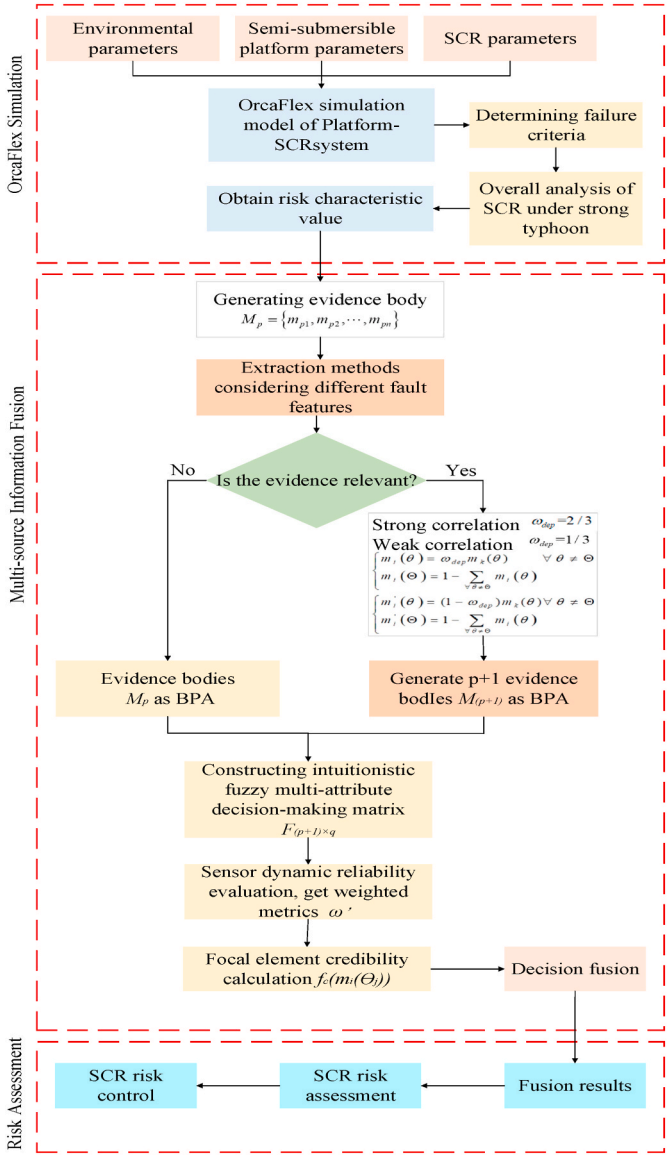


**Fig. 2.** Fig. 2. SCR risk assessment framework.

### 3.1. Construction of BPA

The decision level information fusion algorithm based on intuitionistic fuzzy evidence firstly extracts the fault information from multiple sensors, selects the characteristic fault parameters as the identification framework, generates the basic trust allocation function (BPA), and establishes the reliability matrix. The BPA function is finally generated by considering whether multiple sensors are correlated, that is, homogeneous or heterogeneous sensors.

With $P$ sensors, $q$ class status, $P > 1$ $q > 1$. Then the identification framework $\Theta = \{\theta_1, \theta_2, \ldots, \theta_q\}$.

Let $S = \{s_1, s_2, \cdots, s_q\}$ represent the eigenvector of the measurement data of the sensor, and $s_q$ represent the eigenvalue of the measurement data of the q-th state. Establish corresponding state matrix:

$$X = \begin{bmatrix} X_1 \\ X_2 \\ \vdots \\ X_p \end{bmatrix} = \begin{bmatrix} x_{11} & x_{12} & \cdots & x_{1q} \\ x_{21} & x_{22} & \cdots & x_{2q} \\ \vdots & \vdots & \ddots & \vdots \\ x_{p1} & x_{p2} & \cdots & x_{pq} \end{bmatrix} \tag{7}$$

where $X_P$ is a vector describing the class $q$ state measured by the p-th sensor, and $x_{ij}, \cdots, x_{iq}$ $x_{ij} > 0$ represents the state value measured by the i-th sensor in the class $j$ state; Where, $i = 1, 2, \cdots, p$; $j = 1, 2, \cdots, q$.

Define the parameter distance between $S$ and $X_i$:

$$d_{ij} = \begin{cases} \dfrac{s_j - x_{ij}}{s_j} & i = 1, 2, \cdots, p; j = 1, 2, \cdots, q \\ \Delta d_{ij} & if \quad s_j - x_{ij} \le 0 \end{cases} \tag{8}$$

In order to strictly limit the situation that the initial basic trust function cannot be obtained, when $s_j - x_{ij} \le 0$, an incremental distance $\Delta d_{ij}$ is added to the parameter distance between $S$ and $X_i$. The smaller the distance $d_{ij}$, the greater the possibility of judging that the object is in the corresponding state feature according to the i-th sensor data information. Therefore, the setting of incremental distance will not affect the judgment result if it is within an appropriate range.

Calculate the distance between the eigenvector $S$ of all sensor measurement data and the corresponding state vector $X$, and establish the distance matrix:

$$D = \begin{bmatrix} d_{11} & d_{12} & \cdots & d_{1q} \\ d_{21} & d_{22} & \cdots & d_{2q} \\ \vdots & \vdots & \ddots & \vdots \\ d_{p1} & d_{p2} & \cdots & d_{pq} \end{bmatrix} \tag{9}$$

Therefore, $m_{ij}$ is inversely correlated with $d_{ij}$ and normalized:

$$\sum_{j=1}^{q} m_{ij} = 1 \tag{10}$$

Expressed in matrix form:

$$M = \begin{bmatrix} m_{11} & m_{12} & \cdots & m_{1q} \\ m_{21} & m_{22} & \cdots & m_{2q} \\ \vdots & \vdots & \ddots & \vdots \\ m_{P1} & m_{P2} & \cdots & m_{Pq} \end{bmatrix} = \begin{bmatrix} M_1 \\ M_2 \\ \vdots \\ M_P \end{bmatrix} \tag{11}$$

Then $M_k = \{m_{k1}, m_{k2}, \cdots, m_{kn}\}$ can be used as the reliability value of the k-th sensor for state recognition. $M$ is called the reliability matrix.

If the underlying probability distribution function of multiple focus elements is generated by two evidences from the same source of evidence or based on the same characteristics and attributes, then this focus element is called a correlated focus element and the two pieces of evidence are correlated. For a set of correlated evidence, the percentage of repeated evidence is called correlation and is expressed as $\omega_{dep}$. For a fault diagnosis process where various fault feature information is collected using the same sensor and the fault features are retrieved in the same way, the correlation of the evidence is $\omega_{dep} = 2/3$.This is since

there are three main influencing factors in the process: the sensor, the fault features and the fault feature extraction method (the method of solving the basic probability function). According to these three factors, this paper divides the evidence into eight correlation types, and then classifies the eight correlation types into three types: strong correlation, weak correlation and independent based on prior knowledge, and gives the division of evidence correlation, as shown in Fig. 3.

After obtaining the different correlations, each evidence in each group is decomposed into two independent correlations, respectively.:

$$\begin{cases} m_i(\theta) = \omega_{dep} m_k(\theta) & \forall \theta \neq \Theta \\ m_i(\Theta) = 1 - \sum_{\forall \theta \neq \Theta} m_i(\theta) \end{cases}$$
$$\begin{cases} m_i^{'}(\theta) = \left(1 - \omega_{dep}\right) m_k(\theta) & \forall \theta \neq \Theta \\ m_i^{'}(\Theta) = 1 - \sum_{\forall \theta \neq \Theta} m_i(\theta) \end{cases} \tag{12}$$

Where $m_k(\theta)$ is the initial evidence group extracted from the sensor. The confidence of the i-th evidence of $m_k(\theta)$ is split to obtain two sets of confidence sets, in which $m_i(\theta)(i = 1, 2, \ldots, p)$ is the set based on the confidence of relevant source evidence and $m_i^{'}(\theta)(i = 1, 2, \ldots, p)$ is the set based on the confidence of independent source evidence. For the relevant source evidence set $m_i(\theta)$, average it to obtain:

$$\overline{m}(\theta) = \frac{1}{p} \sum_{i=1}^{p} m_i(\theta) \forall \theta \in D^{\Theta} \tag{13}$$

where, the average confidence $\overline{m}(\theta)$ means that all relevant source evidence is evenly distributed to $\theta$. So far, the number of independent evidence has reached $p + 1$. Then it is applied to the dynamic reliability evaluation of sensors in the next section, and the independent evidence after decorrelation is combined.

### 3.2. Dynamic reliability evaluation of sensors

In this section, a sensor dynamic reliability evaluation method based the intuitionistic fuzzy multi-attribute decision is proposed. Compared with static sensor reliability evaluation without a large amount of a priori information, as well as the influence of environmental factors is considered.

$\Theta = \{\theta_1\ \theta_2\ \ldots\ \theta_q\}$ is the identification framework, $m_1, m_2, \cdots, m_p$ represent $p$ evidence bodies to be combined, $Su_{ij} = \langle \mu_i(\theta_j), \upsilon_i(\theta_j) \rangle$ is intuitionistic fuzzy number, which represents $m_i$'s support for $\theta_j$, and $\mu_i(\theta_j) = m_i(\theta_j), \upsilon_i(\theta_j) = 1 - \mu_i(\theta_j) - \pi_i(x), i = 1, 2, \cdots, q, j = 1, 2, \cdots, p$. The intuitionistic fuzzy multi-attribute decision matrix model of $m$ on $\theta$ is expressed as follows:

$$F = \left(\langle \mu_i(\theta_j), \upsilon_i(\theta_j) \rangle\right)_{q \times p} = \begin{array}{c} \\ \theta_1 \\ \theta_2 \\ \vdots \\ \theta_q \end{array} \begin{array}{c} \begin{array}{cccc} m_1 & m_2 & \cdots & m_p \end{array} \\ \begin{bmatrix} Su_{11} & Su_{21} & \cdots & Su_{p1} \\ Su_{12} & Su_{22} & \cdots & Su_{p2} \\ \vdots & \vdots & \ddots & \vdots \\ Su_{1q} & Su_{2q} & \cdots & Su_{pq} \end{bmatrix} \end{array}$$
$$= \begin{array}{c} \\ \theta_1 \\ \theta_2 \\ \vdots \\ \theta_q \end{array} \begin{array}{c} \begin{array}{cccc} m_1 & m_2 & \cdots & m_p \end{array} \\ \begin{bmatrix} \langle \mu_1(\theta_1), \upsilon_1(\theta_1) \rangle & \langle \mu_2(\theta_1), \upsilon_2(\theta_1) \rangle & \cdots & \langle \mu_p(\theta_1), \upsilon_p(\theta_1) \rangle \\ \langle \mu_1(\theta_2), \upsilon_1(\theta_2) \rangle & \langle \mu_2(\theta_2), \upsilon_2(\theta_2) \rangle & \cdots & \langle \mu_p(\theta_2), \upsilon_p(\theta_2) \rangle \\ \vdots & \vdots & \ddots & \vdots \\ \langle \mu_1(\theta_q), \upsilon_1(\theta_q) \rangle & \langle \mu_2(\theta_q), \upsilon_2(\theta_q) \rangle & \cdots & \langle \mu_p(\theta_q), \upsilon_p(\theta_q) \rangle \end{bmatrix} \end{array} \tag{14}$$

Therefore, the scheme is evaluated under the condition of intuitionistic fuzzy multi-attribute decision-making, and the weight of each attribute in the intuitionistic fuzzy multi-attribute decision-making is equivalent to the dynamic reliability of each sensor.

In the above, the estimation method of attribute weight is used to evaluate the dynamic reliability of evidence in intuitionistic fuzzy multi-attribute decision-making. Let the intuitionistic fuzzy number $\langle \mu_{ij}, \upsilon_{ij} \rangle$ represent the evaluation result of scheme $m_i$ under attribute $\theta_j$, $\langle \mu_{ij}, \upsilon_{ij} \rangle$ and $\langle \mu_{kj}, \upsilon_{kj} \rangle$ are the evaluation results of any two scheme $m_i$ and $m_k$, and let $P^{(j)}_{(m_i \geq m_k)}$ be the possibility that $\langle \mu_{ij}, \upsilon_{ij} \rangle$ is greater than $\langle \mu_{kj}, \upsilon_{kj} \rangle$, then:

$$P^{(j)}_{(m_i \geq m_k)} = \min\left\{1, \max\left\{\frac{1 - \upsilon_{ij} - \mu_{kj}}{\pi_{ij} + \pi_{kj}}, 0\right\}\right\} \tag{15}$$

If the hesitation degree $\pi$ of intuitionistic fuzzy number is zero, it degenerates from intuitionistic fuzzy number to fuzzy number. For two fuzzy numbers $\alpha = [a^L, a^U]$ and $\beta = [b^L, b^U]$ respectively and satisfy $a^L \leq a^U, b^L \leq b^U$, the possibility degree $P_{(\alpha \geq \beta)}$ of $\alpha$ not less than $\beta$ is defined as:

$$P_{(\alpha \geq \beta)} = \min\left\{1, \max\left\{\frac{a^U - b^L}{(a^U - a^L) + \left(b^U - b^L\right)}, 0\right\}\right\} \tag{16}$$

According to the possibility obtained from the above formula, the contrast relationship matrix $P^{(j)}$ between $p$ intuitionistic fuzzy numbers can be established:

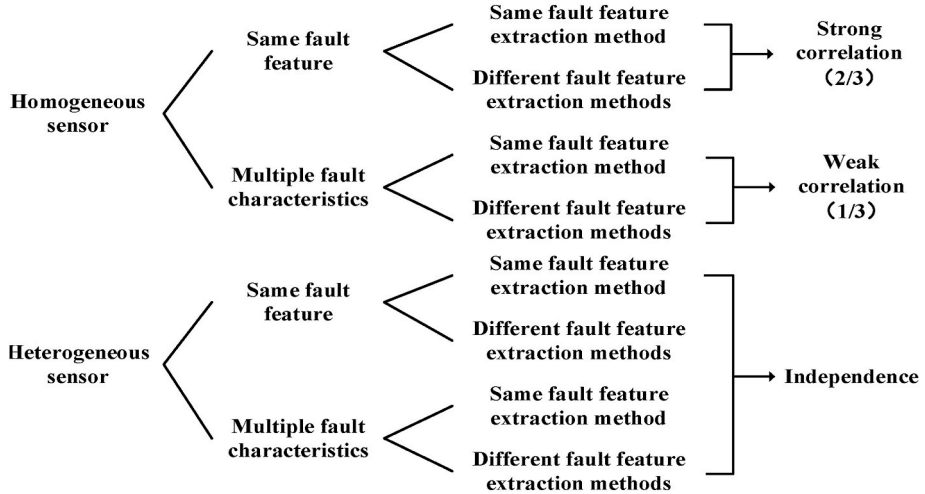


**Fig. 3.** Fig. 3. Division of evidence relevance.

$$P^{(j)}=\begin{pmatrix} P^{(j)}_{(m_1\geq m_1)} & P^{(j)}_{(m_1\geq m_2)} & \cdots & P^{(j)}_{(m_1\geq m_p)} \\ P^{(j)}_{(m_2\geq m_1)} & P^{(j)}_{(m_2\geq m_2)} & \cdots & P^{(j)}_{(m_2\geq m_p)} \\ \vdots & \vdots & \ddots & \vdots \\ P^{(j)}_{(m_p\geq m_1)} & P^{(j)}_{(m_p\geq m_2)} & \cdots & P^{(j)}_{(m_p\geq m_p)} \end{pmatrix} \tag{17}$$

The sum of the k-th row of matrix $P^{(j)}$ can be used as the possibility degree, indicating that $m_k$ is greater than other schemes, so there is

$$P^{(j)}_k=\sum_{m=1}^{p}P^{(j)}_{km},\ k=1,2,\cdots,p \tag{18}$$

Therefore, the weight given to attribute $\theta_j$ by scheme $m_i$ can be expressed as:

$$\omega^{(j)}_i=\frac{P^{(j)}_i}{\sum\limits_{m=1}^{p}P^{(j)}_m} \tag{19}$$

The obtained attribute weight vector can be expressed as:

$$\omega^{(j)}=\left(\omega^{(j)}_1,\omega^{(j)}_2,\cdots,\omega^{(j)}_p\right)^T \tag{20}$$

As the attribute weight vector for making decisions on each scheme, the final ideal weight vector of vector $\omega^{(j)}$ must be the minimum sum of the angles between all vectors $\omega^{(j)}$. The weight vector can be solved by the eigenvalue method. Therefore, the matrix $W=(\omega^{(1)},\omega^{(2)},\cdots,\omega^{(p)})$ is defined, and the eigenvector $\omega$ corresponding to the maximum eigenvalue of the square matrix $WW^T$ is the final ideal weight vector.

The eigenvectors corresponding to the same eigenvalues are not unique, so $\omega$ needs to be normalized:

$$\omega'=\frac{\omega}{\sum\limits_{i=1}^{p}\omega_i} \tag{21}$$

The dynamic reliability weight index of sensor is obtained based on intuitionistic fuzzy multi-attribute decision-making.

### 3.3. Evidence conflict resolution and decision fusion algorithm

1) Improved calculation formula of focal element reliability

Let $m_\omega(\theta_j)$ be the weighted average value, which represents the probability distribution of focal element $\theta_j$ in the $p$ pieces of evidence to be fused, that is:

$$m_\omega(\theta_j)=\sum_{i=1}^{p}\omega'_i m_i(\theta_j) \tag{22}$$

Then the distance between $m_i(\theta_j)$ and $m_\omega(\theta_j)$ can be expressed as:

$$f_d\left(m_i(\theta_j)\right)=\left|m_i(\theta_j)-m_\omega(\theta_j)\right| \tag{23}$$

And the similarity measure between $m_i(\theta_j)$ a and $m_\omega(\theta_j)$ can be described as:

$$f_s\left(m_i(\theta_j)\right)=2m_i(\theta_j)m_\omega(\theta_j)\Big/\left(\left[m_i(\theta_j)\right]^2+\left[m_\omega(\theta_j)\right]^2\right) \tag{24}$$

$f_d(m_i(\theta_j))$ represents the absolute difference of the distance between $m_i(\theta_j)$ and $m_\omega(\theta_j)$, but it still does not fully represent the proportion of the weighted average of the probability assignment in the distance. Therefore, considering the relative distance difference to reflect the credibility of $m_i(\theta_j)$ itself, we can specifically describe the relationship between the probability distribution of focal element $\theta_j$ and the weighted average $m_\omega(\theta_j)$ in the evidence. The relative distance difference can be expressed as:

$$f_{rd}\left(m_i(\theta_j)\right)=\begin{cases}1, \left|m_i(\theta_j)-m_\omega(\theta_j)\right|>m_\omega(\theta_j)\\ \dfrac{\left|m_i(\theta_j)-m_\omega(\theta_j)\right|}{m_\omega(\theta_j)}, \quad else\end{cases} \tag{25}$$

Therefore, the fusion trust function between $m_i(\theta_j)$ and $m_\omega(\theta_j)$ can be expressed as:

$$f^f_s\left(m_i(\theta_j)\right)=\frac{\left(1-f_{rd}\left(m_i(\theta_j)\right)\right)f_s\left(m_i(\theta_j)\right)}{\sum\limits_{i=1}^{p}\left(1-f_{rd}\left(m_i(\theta_j)\right)\right)\sum\limits_{i=1}^{p}f_s\left(m_i(\theta_j)\right)} \tag{26}$$

In order to strengthen the role of evidence weight in conflict information allocation, the credibility of focal element $\theta_j$ in $m_i$ can be defined as follows:

$$f_c\left(m_i(\theta_j)\right)=\frac{\omega'_i f^f_s\left(m_i(\theta_j)\right)}{\sum\limits_{i=1}^{p}\sum\limits_{j=1}^{q}\omega'_i f^f_s\left(m_i(\theta_j)\right)} \tag{27}$$

2) Multi evidence fusion algorithm based on improved hybrid DSm model

It is assumed that the primary focus elements under the identification framework $\Theta$ are compatible, that is $\theta_i\cap\theta_j\neq\varnothing$, indicates that the result of the intersection operation is directly assigned to the corresponding subset. While if the primary focus elements are incompatible with each other, that is $\theta_i\cap\theta_j=\varnothing$, the amount of conflict in the obtained assignment result is assigned in proportion to the conflicting focus elements, which are from the set of single-focus elements and the set of multiple sub-focus elements. $\theta$ represents any focus element, $\theta_i,\theta_j\in\theta$, $i\neq j$, $\theta_u,\theta_\nu$ represents single-focus element, $P_1$ represents singleton focus element set, $\theta_c$ represents multiple sub-focus element, and $P_2$ represents the set of multiple sub-focus elements composed of crossing and uniting.

$$m(\theta)=\begin{cases} m(\theta_u)=m_\cap(\theta_u)+\sum\limits_{\theta_u\cap\theta_\nu=\varnothing}d_\cap\left(\dfrac{f_c(m_i(\theta_u))m_i(\theta_u)m_i(\theta_u)m_j(\theta_\nu)}{f_c(m_i(\theta_u))m_i(\theta_u)+f_c\left(m_j(\theta_\nu)\right)m_j(\theta_\nu)}+\dfrac{f_c\left(m_j(\theta_u)\right)m_j(\theta_u)m_j(\theta_u)m_i(\theta_\nu)}{f_c\left(m_j(\theta_u)\right)m_j(\theta_u)+f_c(m_i(\theta_\nu))m_i(\theta_\nu)}\right)\\ m(\theta_c)=m_\cap(\theta_c)+\sum\limits_{\substack{\theta_i\cap\theta_j=\varnothing\\ \theta_i\cup\theta_j=\theta_c}}(1-d_\cap)\left(m_i(\theta_i)m_j\left(\theta_j\right)\right)\\ d_\cap=\dfrac{1}{d(\theta_\cap)}\end{cases} \tag{28}$$

In the above formula, $\theta_u, \theta_\nu \in P_1$, and $u, \nu = 1, 2, \ldots, n, u \neq \nu$, $n$ is the number of focal elements. $\theta_c \in P_2$, Where $m_\cap(\theta_u)$ represents the focal element of $\theta_i \cap \theta_j = \theta_u$, $m_\cap(\theta_c)$ represents the focus element of $\theta_i \cap \theta_j = \theta_c$, and $d(\theta_\cap)$ represents the amount of conflict focus elements that are assigned. The above information fusion algorithm is referred to as the IFS-DSm algorithm. Fig. 2 shows the SCR risk assessment process framework under OrcaFlex simulation environment based on the information fusion algorithm proposed in this paper.

## 4. Risk assessment of SCR based on information fusion

During the period 1992 to 2005, hundreds of risers in the Gulf of Mexico were damaged to varying degrees by hurricanes. To make the example research more realistic, this section was opted for risk assessment of SCRs with 100-year, 500- year and 1000-year tropical cyclones in the South China Sea. First, the SCR was modeled and overall strength analysis was performed using OrcaFlex. After that, the corresponding risk characteristic values are acquired according to the three failure modes to be evaluated, that are Maximum Bending Stress, Maximum Effective Tension and Maximum von Mises Stress. Finally, the SCR risk is estimated according to the proposed information fusion method.

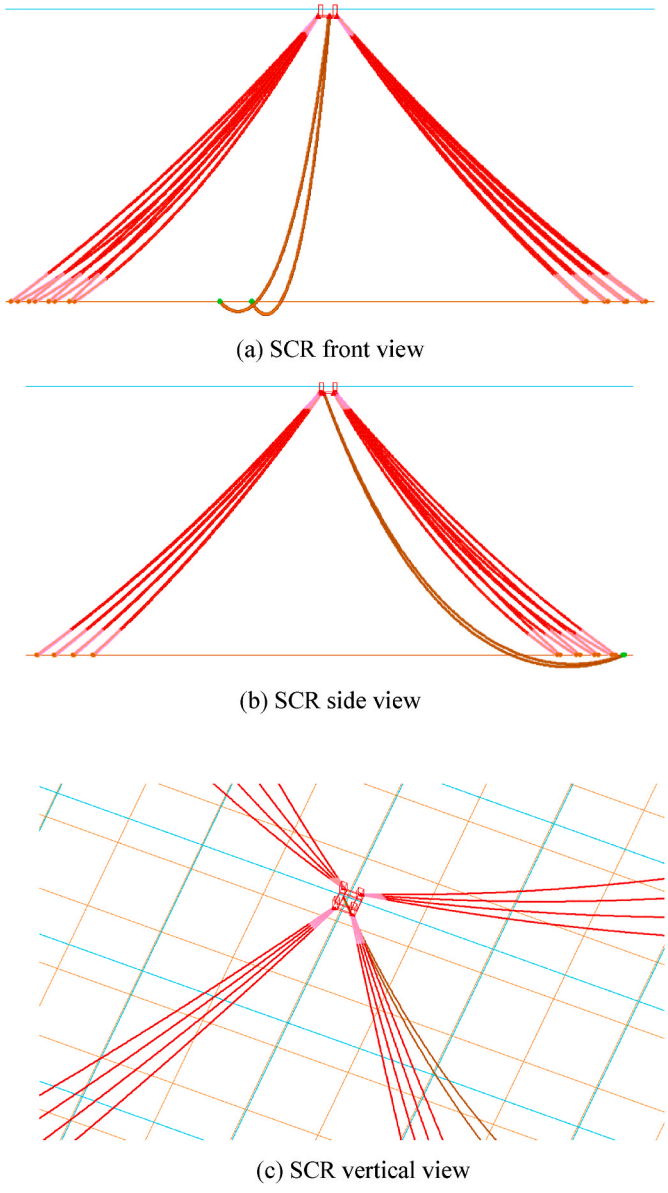


**Fig. 4.** Fig. 4. SCR model.

**Table 1**
Main parameters of riser.

| parameter | numerical value | unit | parameter | numerical value | unit |
|---|---|---|---|---|---|
| Internal diameter | 0.297 | m | Axial stiffness | 5209 | MN |
| External diameter | 0.324 | m | Bending stiffness | 57.913 | $MNm^2$ |
| Total length | 2397.26 | m | Torsional stiffness | 44.548 | $MNm^2$ |
| Dry weight | 0.201 | $T/m^3$ | Material density | 7.850 | $T/m^3$ |
| Wet weight | 0.116 | $T/m^3$ | Design tension | 2571 | KN |

**Table 2**
Marine environmental parameters.

| parameter | significant wave height (m) | Peak period (s) | γ | wind speed (m/s) | Surface velocity (m/s) |
|---|---|---|---|---|---|
| 100-year | 12.61 | 14.6 | 2.4 | 44.429 | 1.68 |
| 500-year | 14.26 | 15.1 | 2.4 | 48.031 | 1.83 |
| 1000-year | 15.91 | 15.6 | 2.4 | 51.633 | 1.99 |

### 4.1. Establishment of SCR simulation model

AQWA software was first applied to calculate the hydrodynamic response of the semi-submersible platform, and then was implemented into OrcaFlex software. After the simulation model of the SCR riser is developed in OrcaFlex and the overall analysis is conducted. Among the loads involved in the overall analysis are the environmental loads under strong typhoon.

As an example, the development facility of an oil and gas field in the South China Sea consists of a deep-water semi-submersible platform, SCR, subsea production system and subsea pipeline. The water depth of the sea where the oil and gas field is located is 1422 m. The semi-submersible platform is fixed by 16 mooring cables, and the SCR is attached from the platform through a flexible joint, as shown in Fig. 4. The dimensions of the riser are shown in Table 1.

The relevant parameters of the marine environment where the target SCR is located are shown in Table 2. Among them, the wave type is JONSWAP spectrum, and the wind speed is the average wind speed measured within 1 h at 10m above the sea surface.

### 4.2. Overall strength analysis of riser structure

The flex joint connection point and the touchdown point of SCR are susceptible to fatigue failure. This is due to the large alternating loads and cyclic stresses, which should be monitored as critical areas. In addition, due in part to corrosion and alternating stress, there is a need to monitor the risers as they are prone to buckling failure in the offshore splash zone. Fig. 5 shows the layout of SCR monitoring system of semi-submersible platform, and Table 3 shows the number, location and monitoring parameters of these virtual sensors. The sensors in suspension area are employed to measure effective tension, the strain sensors in touchdown zone are implemented to measure bending stress, and the sensors in splash area is required to measure Max von Mises stress.

Check the combined stress of riser according to the allowable stress method specified in API RP 2RD specification, obtain von Mises stress according to von Mises combined stress formula, and verify that it does not exceed the allowable stress. API RP 2RD specification gives the corresponding value of allowable stress, as shown in Table 4.

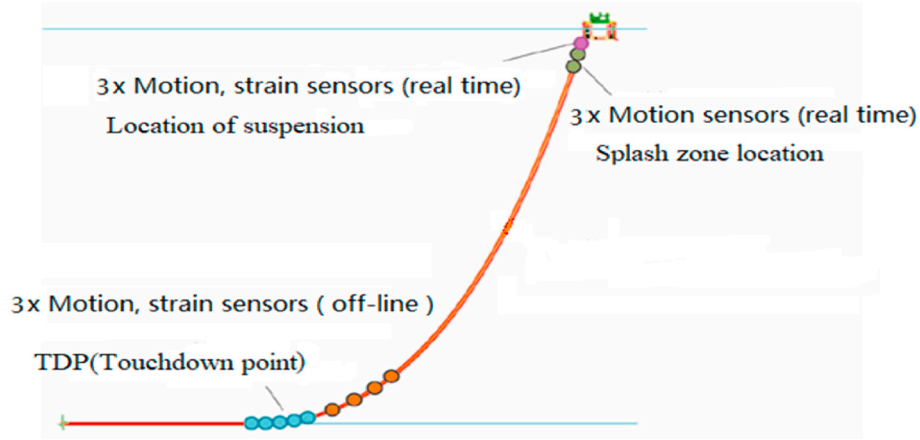


**Fig. 5.** Fig .5. Layout of SCR monitoring system.

**Table 3**
Parameters of the virtual sensor.

| Installation Location | No. of sensors | type of sensors | Main monitoring parameters |
|---|---|---|---|
| Location of suspension | 3 | Motion, strain, and acceleration sensors | Maximum effective tension |
| Splash zone location | 3 | Motion, strain, and acceleration sensors | Allowable stress |
| Touchdown point | 3 | Motion, strain, and acceleration sensors | Maximum bending stress |

The riser is made of X65 steel, the yield strength is 450 MPa, and the allowable stress is 360 MPa under extreme working conditions. The failure judgment criteria of riser are shown in Table 5 below:

Multiple sensors are installed at the bend zone to the touchdown zone of the SCR, with the maximum bending stress at the touchdown point. The position 10 m below the top of the SCR is to be chosen in order to imitate the location of the real SCR in the ocean splash zone.

As the semi-submersible platform moves in response to strong typhoons, it can cause failure problems in the SCR structure. Consequently, the strength of the riser structure is estimated to ascertain the weak areas of the riser structure. Three groups of diverse working conditions were randomly selected to obtain effective tension Max von Mises stress and bending stress of the riser under different periods of typhoon, as shown in the following figure.

From Fig. 6(a), (b), and (c), the effective tension of the SCR under the three typhoons varies approximately the same. The movement of the upper platform induced with environmental load altered only the tension value. The tension at the top connection point is the largest. The tension value would not exceed the design tension of the riser, so it could be considered safe here. Nevertheless, the tension values here are larger,

**Table 4**
Allowable stress standard.

| Stress type | Allowable stress |
|---|---|
| Primary membrane stress | $K\sigma_m$ |
| Primary membrane stress + bending stress | $1.5K\sigma_m$ |
| Primary membrane stress + bending stress + secondary stress | $3.0K\sigma_m$ |
| Primary membrane stress + bending stress + secondary stress range | Based on S–N fatigue curve |
| Average bearing stress | $0.9K\sigma_m$ |

$K$ is a function of the severity and frequency of the working conditions studied, including 1.0 of the working conditions, 1.2 of the extreme conditions and 1.5 of the survival conditions. $\sigma_m = 2/3 \times \sigma_y$, $\sigma_y$ is the yield strength of the material.

**Table 5**
Criteria for riser failure.

| Potential failure location | Evaluation parameters | Failure parameters |
|---|---|---|
| Location of suspension area joint connection point | Maximum effective tension | 2571 KN |
| Splash zone location | Allowable stress | 360 MPa |
| Touchdown point | Maximum bending stress | 360 MPa |

so the stability is poor and special attention should be observed.

The generic SCR top flexible riser has different stiffness at each torsional angle, which is designed to eliminate the stress concentration phenomenon generated by various complex forces. Due to the complex physical characteristics of the flexible riser, this OrcaFlex simulation model reduces the flexible riser to a steel tube, which causes the top of the riser to be subjected to a large amount of stress, as can be seen by Fig. 7. As the water depth increased, the bending stresses in the riser decreased sharply. In the submerged part of the riser, the bending stress fluctuated in a small range, with the maximum bending stress at the touchdown point.

Comparing the maximum von Mises stresses under the three typhoons (see Fig. 8), the stresses in the riser suspension zone to the splash zone are slightly higher, and a significant stress concentration appears at the top, which is resulted by the model adopting fixed-end connection. The maximum von Mises stress wavered significantly in the touchdown zone due to the soil limitation.

### 4.3. SCR risk assessment based on IFS-DSm algorithm

The effective tension, bending stress and maximum von Mises stress obtained by the sensor in a strong typhoon environment with a recurrence period of one thousand years are shown in Table 6 (see Table 7).

The fault measured at the position of the joint zone is the failure fracture at the top flexible joint area ($\theta_1$), the fault measured at the position of the riser in the touchdown zone is the fatigue fracture failure at the touchdown point ($\theta_2$), and the fault measured at the position of the riser in the splash zone is the buckling failure ($\theta_3$). Considering that the most likely multiple coupling faults of SCR are predominantly joint breakage at suspension point and fatigue fracture at touchdown point, and thus $\theta_1 \cap \theta_2 \neq \varnothing$, other coupling faults are set as $\varnothing$. Firstly, the evidence body is generated by IFS-DSm algorithm:

The sensors are regarded as combined sensors. The failure features are derived from the structural stresses, the correlation degree of the divided sensors is 2/3, and the $BPA_S$ of the three fault modes are obtained as shown in Table 8.

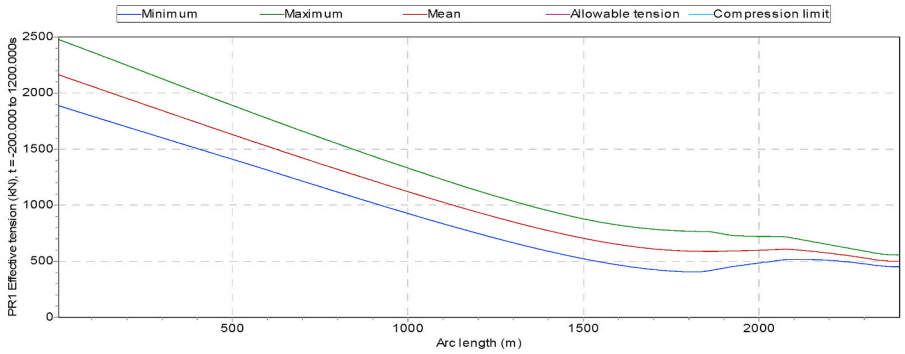


(a) Effective tension distribution of riser under 100-year typhoon

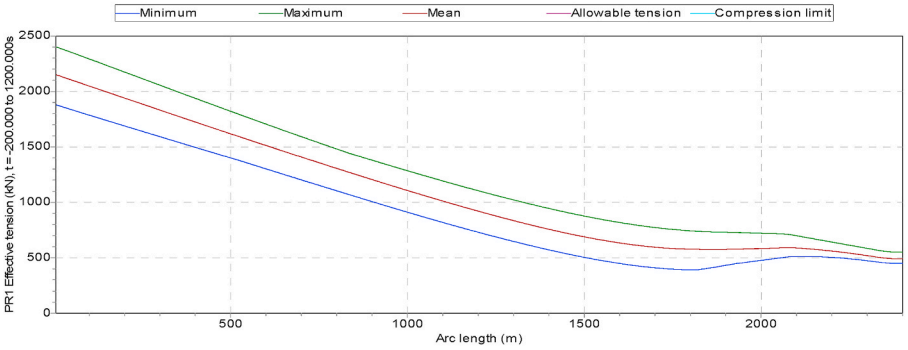


(b) Effective tension distribution of riser under 500-year typhoon

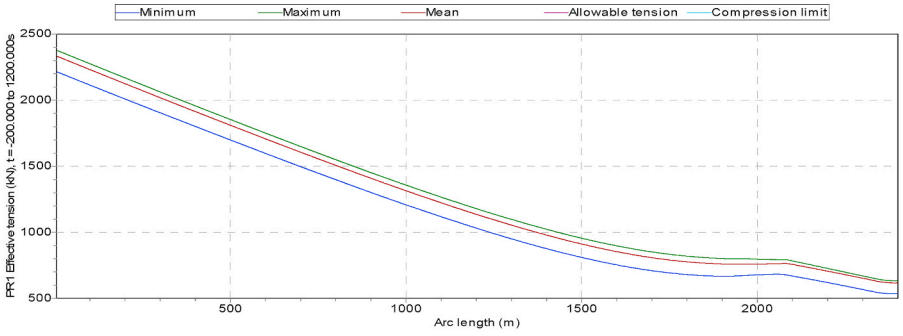


(c) Effective tension distribution of riser under 1000-year typhoon

**Fig. 6.** Fig. 6. Effective tension distribution of riser under different typhoons.

Next, the evidence dynamic reliability evaluation is carried out according to the above obtained failure mode BPA function. Firstly, the following intuitionistic fuzzy multi-attribute decision-making model is established:

$$F = \begin{array}{c} \\ \theta_1 \\ \theta_2 \\ \theta_3 \end{array} \begin{array}{c} \begin{array}{cccc} \mathrm{m}_1 & \mathrm{m}_2 & \mathrm{m}_3 & \mathrm{m}_4 \end{array} \\ \begin{pmatrix} \langle 0.35, 0.31\rangle & \langle 0.28, 0.38\rangle & \langle 0.43, 0.23\rangle & \langle 0.18, 0.16\rangle \\ \langle 0.04, 0.63\rangle & \langle 0.20, 0.46\rangle & \langle 0.10, 0.56\rangle & \langle 0.06, 0.28\rangle \\ \langle 0.28, 0.39\rangle & \langle 0.18, 0.49\rangle & \langle 0.13, 0.54\rangle & \langle 0.10, 0.24\rangle \end{pmatrix} \end{array}$$

According to Eqs. (15) and (17), the comparison relationship matrix between the evaluation results of the three fault modes under different attributes is obtained:

$$P^{(1)} = \begin{pmatrix} 0.5 & 0.604 & 0.380 & 0.508 \\ 0.396 & 0.5 & 0.276 & 0.438 \\ 0.620 & 0.724 & 0.5 & 0.588 \\ 0.492 & 0.562 & 0.412 & 0.5 \end{pmatrix}$$

$$P^{(2)} = \begin{pmatrix} 0.5 & 0.253 & 0.402 & 0.314 \\ 0.747 & 0.5 & 0.649 & 0.479 \\ 0.598 & 0.351 & 0.5 & 0.380 \\ 0.686 & 0.521 & 0.620 & 0.5 \end{pmatrix}$$

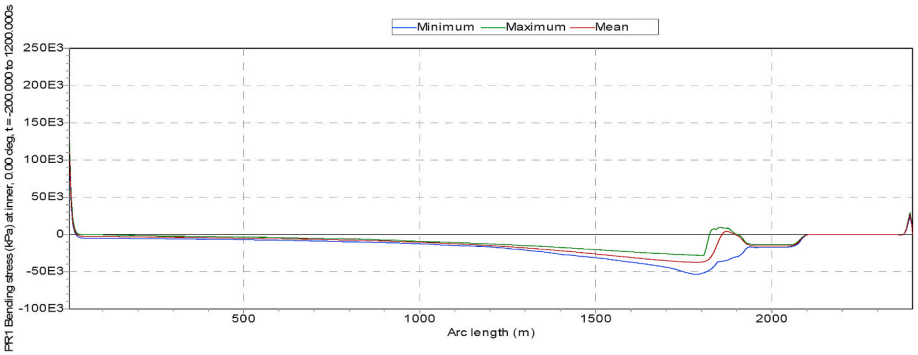


(a) Bending stress distribution of riser under 100-year typhoon

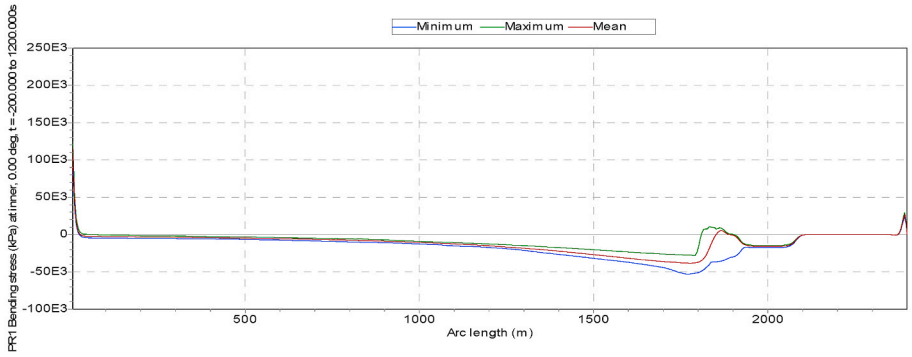


(b) Bending stress distribution of riser under 500-year typhoon

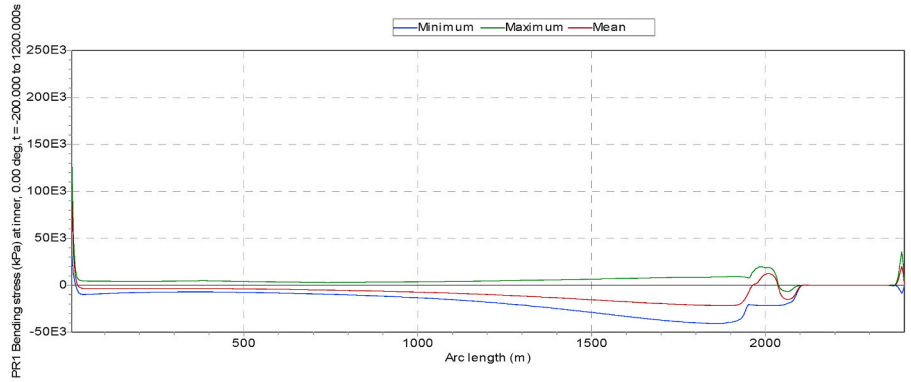


(c) Bending stress distribution of riser under 1000-year typhoon

**Fig. 7.** Fig .7. Bending stress distribution of riser under different typhoons.

$$P^{(3)} = \begin{pmatrix} 0.5 & 0.642 & 0.718 & 0.511 \\ 0.358 & 0.5 & 0.575 & 0.416 \\ 0.282 & 0.425 & 0.5 & 0.366 \\ 0.489 & 0.584 & 0.634 & 0.5 \end{pmatrix}$$

Next, the following can be obtained through Eq. (18):

$$P_1^{(1)} = 1.99, P_2^{(1)} = 1.61, P_3^{(1)} = 2.43, P_4^{(1)} = 1.97$$

$$P_1^{(2)} = 1.47, P_2^{(2)} = 2.37, P_3^{(2)} = 1.83, P_4^{(2)} = 2.33$$

$$P_1^{(3)} = 2.37, P_2^{(3)} = 1.85, P_3^{(3)} = 1.57, P_4^{(3)} = 2.21$$

According to Eqs. (19) and (20), the estimation of attribute weight vector for three fault modes can be obtained as follows:

$$\omega^{(1)} = (0.2491, 0.2012, 0.3039, 0.2458)^T$$

$$\omega^{(2)} = (0.1836, 0.2968, 0.2287, 0.2909)^T$$

$$\omega^{(3)} = (0.2964, 0.2311, 0.1966, 0.2759)^T$$

Construct the matrix according to the above weight vector:

$$W = \left[\omega^{(1)}, \omega^{(2)}, \omega^{(3)}, \omega^{(4)}\right] = \begin{bmatrix} 0.2491 & 0.1836 & 0.2964 \\ 0.2012 & 0.2968 & 0.2311 \\ 0.3039 & 0.2287 & 0.1966 \\ 0.2458 & 0.2909 & 0.2759 \end{bmatrix}$$

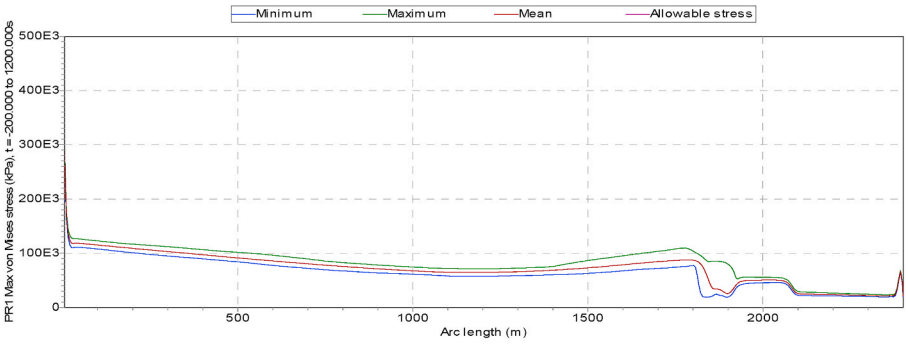


(a) Max von Mises stress distribution of riser under 100-year typhoon

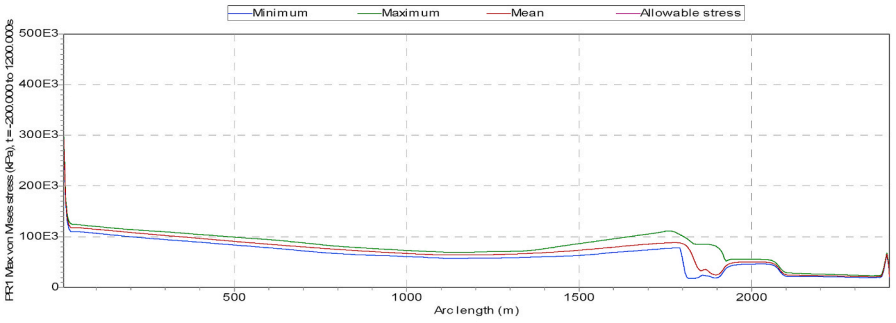


(b) Max von Mises stress distribution of riser under 500-year typhoon

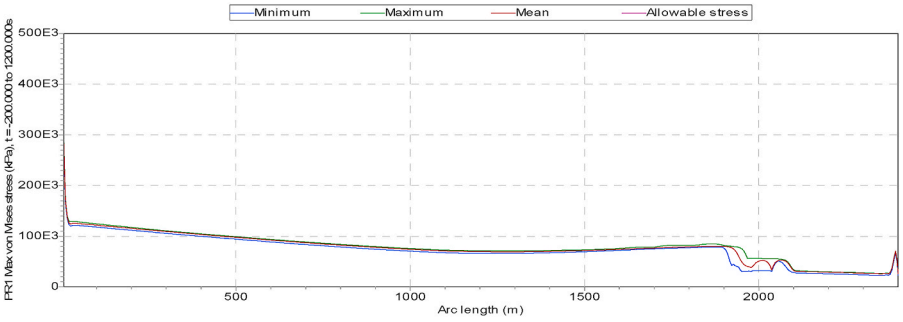


(c) Max von Mises stress distribution of riser under 1000-year typhoon

**Fig. 8.** Max von Mises stress distribution of riser under different typhoons.

**Table 6**
Measurement data of riser under 1000-year typhoon.

| location<br>Sensors | Joint point zone | touchdown zone | Splash zone |
|---|---|---|---|
| m1 | 2377.53 KN | 807.2873 KN | 2323.2661 KN |
| m2 | 131.418 Mpa | 41.793 Mpa | 1.386 Mpa |
| m3 | 293.708 Mpa | 84.893 Mpa | 139.909 Mpa |

**Table 7**
Generated evidence volume data.

| sensors | $\theta_1$ | $\theta_2$ | $\theta_3$ |
|---|---|---|---|
| m1 | 0.528917602 | 0.058019477 | 0.413062921 |
| m2 | 0.424493671 | 0.304932363 | 0.270573966 |
| m3 | 0.64843663 | 0.156252517 | 0.195310854 |

**Table 8**
BPA of three failure modes.

| sensors | θ1 | θ2 | θ3 | Θ |
|---|---|---|---|---|
| m1 | 0.3526 | 0.0387 | 0.2754 | 0.3333 |
| m2 | 0.2830 | 0.2033 | 0.1804 | 0.3333 |
| m3 | 0.4323 | 0.1042 | 0.1302 | 0.3333 |
| m4 | 0.1780 | 0.0577 | 0.0977 | 0.6667 |

$$S = WW^T = \begin{bmatrix} 0.184 & 0.173 & 0.176 & 0.196 \\ 0.173 & 0.182 & 0.174 & 0.200 \\ 0.176 & 0.174 & 0.183 & 0.195 \\ 0.196 & 0.200 & 0.195 & 0.221 \end{bmatrix}$$

The maximum eigenvalue of the calculated square matrix $S$ is 0.7517, and the corresponding eigenvector is:

$$\omega = [-0.48542018 \quad -0.48565587 \quad -0.485415 \quad -0.54118195]^T$$

**Table 9**
Risk assessment results of steel catenary riser under 1000-year typhoon.

| Fusion results | $m_1 \oplus m_2$ | $m_1 \oplus m_2 \oplus m_3$ | $m_1 \oplus m_2 \oplus m_3 \oplus m_4$ |
|---|---|---|---|
| | IFS-DSm | IFS-DSm | IFS-DSm |
| $m(\theta_1)$ | 0.3590 | 0.3814 | 0.3662 |
| $m(\theta_2)$ | 0.0888 | 0.0597 | 0.0499 |
| $m(\theta_3)$ | 0.2562 | 0.2112 | 0.2032 |
| $m(\theta_1 \cap \theta_2)$ | 0.0826 | 0.1733 | 0.2096 |
| $m(\theta_1 \cup \theta_3)$ | 0.0708 | 0.1023 | 0.1056 |
| $m(\theta_2 \cup \theta_3)$ | 0.0315 | 0.0296 | 0.0288 |
| $m(\theta_3 \cup (\theta_1 \cap \theta_2))$ | – | 0.0054 | 0.0120 |
| $m(\Theta)$ | 0.1111 | 0.0370 | 0.0247 |
| Risk assessment results | $\theta_1$ | $\theta_1$ | $\theta_1$ |

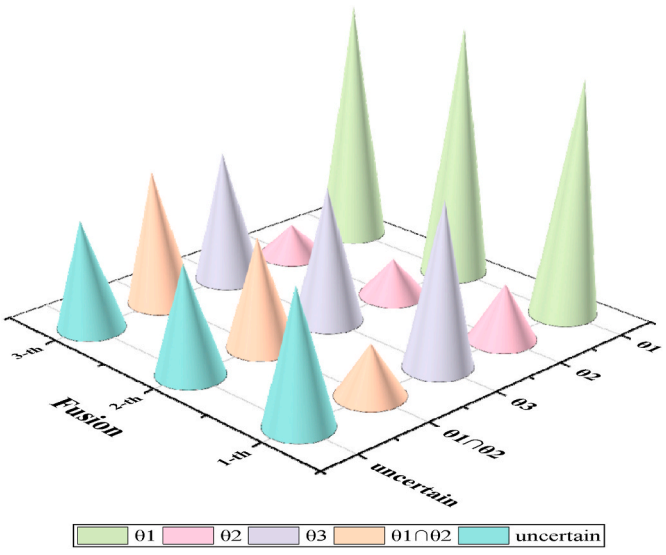


**Fig. 9.** Fig. 9. Risk probability of riser under 1000-year wind.

Normalize $\omega$ to obtain the dynamic reliability weight $\omega'$ of the evidence:

$$\omega' = [0.243 \quad 0.243 \quad 0.243 \quad 0.271]^T$$

Then, according to Eqs. (22)–(27), the credibility of different focal elements can be obtained, and the correction of conflict evidence is realized. Finally, the risk assessment results of different faults in the environment of Millennium strong typhoon can be obtained by decision fusion of different evidence information according to Eq. (28), as shown in Table 9.

From the fusion results in Fig. 9, The final risk assessment result is that $\theta_1$ has the greatest possibility of risk. Secondly, the evaluation results show that the probability of coupling failure of $\theta_1$ and $\theta_2$ in the third fusion is further increasing, reaching 0.2096, slightly greater than the probability of failure of $\theta_3$. The evaluation results always believe that the probability of $\theta_2$ occurring alone is very small, and all the probability of $\theta_2$ reduction is assigned to coupling fault $\theta_1 \cap \theta_2$. The total uncertain probability of failure is 0.1711.

**Table 10**
Risk assessment results of steel catenary riser under 100-year typhoon.

| Fusion results | $m_1 \oplus m_2$ | $m_1 \oplus m_2 \oplus m_3$ | $m_1 \oplus m_2 \oplus m_3 \oplus m_4$ |
|---|---|---|---|
| | IFS-DSm | IFS-DSm | IFS-DSm |
| $m(\theta_1)$ | 0.3370 | 0.3656 | 0.3515 |
| $m(\theta_2)$ | 0.0817 | 0.0569 | 0.0478 |
| $m(\theta_3)$ | 0.2844 | 0.2295 | 0.2218 |
| $m(\theta_1 \cap \theta_2)$ | 0.0784 | 0.1674 | 0.2015 |
| $m(\theta_1 \cup \theta_3)$ | 0.0725 | 0.1072 | 0.1102 |
| $m(\theta_2 \cup \theta_3)$ | 0.0348 | 0.0317 | 0.0305 |
| $m(\theta_3 \cup (\theta_1 \cap \theta_2))$ | – | 0.0048 | 0.0119 |
| $m(\Theta)$ | 0.1111 | 0.0370 | 0.0247 |

**Table 11**
Risk assessment results of steel catenary riser under 500-year typhoon.

| Fusion results | $m_1 \oplus m_2$ | $m_1 \oplus m_2 \oplus m_3$ | $m_1 \oplus m_2 \oplus m_3 \oplus m_4$ |
|---|---|---|---|
| | IFS-DSm | IFS-DSm | IFS-DSm |
| $m(\theta_1)$ | 0.3282 | 0.3582 | 0.3438 |
| $m(\theta_2)$ | 0.0887 | 0.0604 | 0.0509 |
| $m(\theta_3)$ | 0.2858 | 0.2300 | 0.2223 |
| $m(\theta_1 \cap \theta_2)$ | 0.0786 | 0.1706 | 0.2056 |
| $m(\theta_1 \cup \theta_3)$ | 0.0714 | 0.1065 | 0.1092 |
| $m(\theta_2 \cup \theta_3)$ | 0.0362 | 0.0325 | 0.0316 |
| $m(\theta_3 \cup (\theta_1 \cap \theta_2))$ | – | 0.0047 | 0.0120 |
| $m(\Theta)$ | 0.1111 | 0.0370 | 0.0247 |

The highest probability of $\theta_1$ occurrence in triple fusion is due to the adoption of fixed end connections at the joints, and this will create significant stress concentrations. In practice, a flexible joint will be employed at the top of the SCR, which is utilized to remove the stress concentration. By considering the limitations of the model, it can be assumed that the coupled damage of fracture damage at the joint and short-term fatigue damage at the touchdown point of the riser is most likely to appear simultaneously in the 1000-year typhoon environment. As shown in Fig. 10, the fatigue life of the riser shows that the joint and the touchdown point have the shortest life, which verifies the correctness of the risk assessment results.

Similarly, the results of SCR risk assessment based on IFS-DSm algorithm are shown in Table 10 and Table 11 below.

The information fusion shows a consistent pattern of behavior for the various failure risk probabilities in the two different typhoon environments, which is seen in Fig. 11.

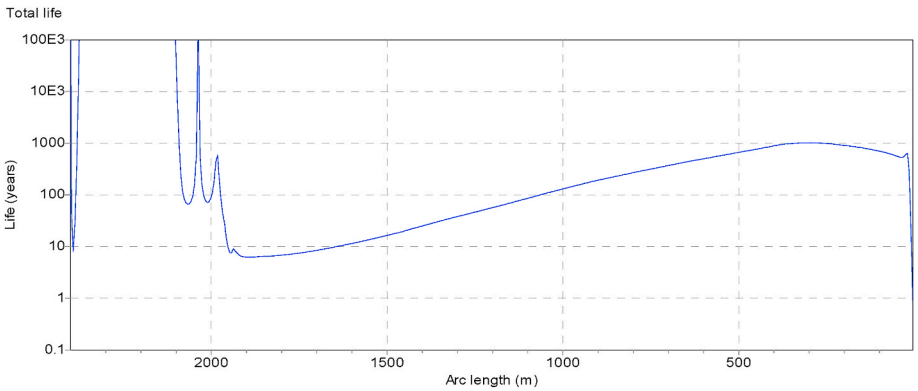


**Fig. 10.** Fig. 10. Distribution diagram of fatigue life analysis under Millennium typhoon.

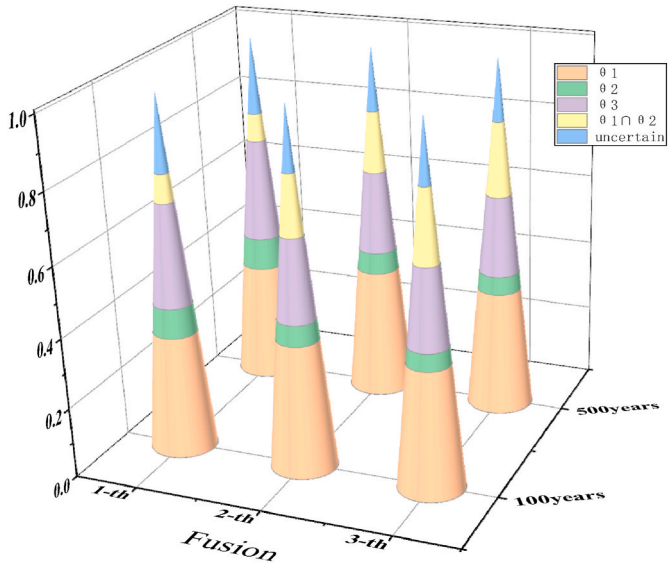


**Fig. 11.** Comparison of riser risk probability under typhoon in two periods.

The final fusion results showed the highest probability of $\theta_1$ risk. Next is flexural failure. It is attributed to the corrosion of SCR by air and seawater in the splash zone, which deteriorates the material performance. In addition, buckling failure can also occur due to the frequent action of wave and tidal forces. Meanwhile, the results of information fusion show that the riser has the least possibility of short-term fatigue fracture at the touchdown point. When short-term fatigue fracture of the riser occurs at the touchdown point, it must be accompanied by coupled damage of fracture damage at the joint. As a result, fracture failure at the joint is most likely to occur under the 100-year and 500-year typhoon environments without accounting for the effect of model accuracy.

Reference (Eom, 2013) in the 100-year strong typhoon environment, the SCR failure mode is evaluated by checking the magnitude and frequency of stress and strain. In the finite element simulation, the dynamic response characteristics of riser caused by the coupling motion of floating structure and the motion characteristics of SCR contact area are studied. According to the literature, the riser suspension point and touchdown end are the most noteworthy locations prone to fatigue. However, this risk assessment method only considers the long-term impact of extreme working conditions on the riser, and does not consider whether the stress peak under short-term working conditions will cause damage to the riser. In comparison, this paper uses the sensor monitoring data to carry out accurate and dynamic risk assessment of SCR, and considers the impact of stress peak on the opposite pipe under short-term working conditions. The risk assessment results are reasonable compared with the reference.

### *4.4. SCR risk control*

In accordance with the above risk assessment results, SCR is most prone to suspension point fracture failure and touchdown point fatigue failure. According to the quantitative risk assessment results of SCR failure mode, corresponding risk control strategies are formulated, which are conducive to the safe and reliable operation of the riser during its service life.

1) The more rigid the joint in the suspension zone, the more likely it is to produce stress concentration. Consequently, the selection of flexible joints with suitable stiffness is conducive to reducing the fatigue damage resulted from stress, thus reducing the occurrence of fracture failure accidents at the joint.
2) The fatigue damage of the touchdown point is primarily affected by the motion of the floating platform and the stiffness of seabed. The stress state of the touchdown zone can be improved by increasing the wall thickness of the riser touchdown zone, optimizing the welding process of the riser touchdown zone and installing buoyancy devices, so as to reduce the occurrence of short-term fatigue failure accident at the touchdown point.

## 5. Conclusion

In this paper, a decision level information fusion algorithm is proposed. The algorithm generates the corresponding evidence bodies through the known fault theory values and the characteristic values measured by sensors, and obtains the BPA function with respect to the correlation between the sensors. It then uses the obtained BPA function to construct an intuitive fuzzy multi-attribute decision matrix, receives the weights of different evidence sources and commutes them to implement the dynamic reliability evaluation of the evidence. At the last, the conflicts between the acquired evidence are addressed and the decision-level fusion is accomplished by an improved DSm theory fusion algorithm. The algorithm is adopted for SCR risk assessment.

Simulation modeling was performed in OrcaFlex with three SCR failure modes with 100-year, 500-year and 1000-year strong typhoons as environmental loads. The proposed information fusion algorithm is evaluated for the risk of SCR based on three indicators: effective tension, bending stress and maximum von Mises stress. Simulation modeling was performed in OrcaFlex with three SCR failure modes with 100-, 500- and 1000-year strong typhoons as environmental loads. The proposed information fusion algorithm is evaluated for the risk of SCR based on three indicators: effective tension, bending stress and maximum von Mises stress. The assessment results show that the risk probability of fracture failure at the joint in the suspension zone is the largest in the 100-year and 500-year strong typhoon environments, and the coupled risk probability of fracture at the joint and short-term fatigue failure at the touchdown point is the largest in the 1000-year strong typhoon environment, without accounting for the effects of model experiments. Lastly, appropriate risk control strategies are proposed based on the risk assessment results.

## CRediT authorship contribution statement

**Peijie Yang:** Methodology, Data curation, Formal analysis, Writing – original draft. **Lusheng Jia:** Resources. **Zhuang Kang:** Supervision. **Jichuan Kang:** Conceptualization, Writing – review & editing.

## Declaration of competing interest

The authors declare that they have no known competing financial interests or personal relationships that could have appeared to influence the work reported in this paper.

## Acknowledgements

This work is supported by the Specialized Research Project for LS17-2 Semi-submersible Production Platform (LSZX-2020-HN-05-0405), the National Natural Science Foundation of China (Grant No. 52101305), the Fundamental Research Funds for Central Universities (Grant No. 3072021CF0101).

## References

Abhulimen, K., 2009. Model for risk and reliability analysis of complex production systems: application to FPSO/flow-Riser system. Comput. Chem. Eng. 33 (7), 1306–1321.

Alzbutas, R., Iešmantas, T., Povilaitis, M., Vitkutė, J., 2014. Risk and uncertainty analysis of gas pipeline failure and gas combustion consequence. Stoch. Environ. Res. Risk Assess. 28 (6), 1431–1446.

Cheng, Y., Tang, L., Fan, T., 2020. Dynamic analysis of deepwater steel lazy wave riser with internal flow and seabed interaction using a nonlinear finite element method. Ocean Eng. 209 (4), 107498.
Dezert, J., 2002. Foundations for a new theory of plausible and paradoxical reasoning. Inf. Secur. J. 12 (1), 26–30.
Ebunuoha, C., Ossia, C., 2017. Steel catenary riser fatigue life prediction using linearized hydrodynamic models. World J. Eng. Technol. (4), 564–573, 05.
Elosta, Hany, 2013. Reliability-based Fatigue Analysis of Steel Catenary Riser with Seabed Interaction. University of Strathclyde.
Eom, T., 2013. Assessment of Global Buckling and Fatigue Life for Steel Catenary RIser by Hull-Riser-Mooring Coupled Dynamic Analysis Program. Texas A & M University. Master's thesis.
Fu, J., Yang, H., 2010. Fatigue characteristic analysis of deepwater steel catenary risers at the touchdown point. China Ocean Eng. 024 (002), 291–304.
Gao, Y., Wang, X., Xiong, Y., Li, Z., Zhi, Z., 2017. Dynamic response and fatigue damage analysis of a steel catenary riser at the touchdown point considering seabed contact. Chin. J. Comput. Mech. 34 (6), 704–711.
Garg, H., Rani, D., 2020. Novel aggregation operators and ranking method for complex intuitionistic fuzzy sets and their applications to decision-making process. Artif. Intell. Rev. 53 (7).
Gong, Y., Su, X., Qian, H., Yang, N., 2018. Research on fault diagnosis methods for the reactor coolant system of nuclear power plant based on D-S evidence theory. Ann. Nucl. Energy 112, 395–399.
Guo, X., Ji, J., Khan, F., Ding, L., Tong, Q., 2021. A novel fuzzy dynamic Bayesian network for dynamic risk assessment and uncertainty propagation quantification in uncertainty environment. Saf. Sci. 141, 105285.
Hu, X., Zhou, C., Duan, M., An, C., 2014. Reliability analysis of marine risers with narrow and long corrosion defects under combined loads. Petrol. Sci. 11, 139–146.
Khakzad, N., 2019. System safety assessment under epistemic uncertainty: using imprecise probabilities in bayesian network. Saf. Sci. 116, 149–160.
Khan, R., Ahmad, S., 2007. Safety of a deep water marine riser under random loads. Marit. Eng. 160, 175–183.
Komachi, Y., Mazaheri, S., Tabeshpour, M., 2018. Wake and structure model for simulation of cross-flow/in-line vortex induced vibration of marine risers. J. Vibro. Eng. 20 (1).
Li, H., Díaz, H., Guedes Soares, C., 2021. A failure analysis of floating offshore wind turbines using AHP-FMEA methodology. Ocean Eng. 234, 109261.
Li, H., Haung, C.G., Guedes Soares, C., 2022. A real-time inspection and opportunistic maintenance strategies for floating offshore wind turbines. Ocean Eng. 256, 111433.
Masoumi, Z., Van, L., Genderen, J., Maleki, J., 2019. Fire risk assessment in dense urban areas using information fusion techniques. ISPRS Int. J. Geo-Inf. 8 (12), 579.
Misuri, A., Khakzad, N., Reniers, G., Cozzani, V., 2019. Tackling uncertainty in security assessment of critical infrastructures: Dempster-Shafer Theory vs. Credal Sets Theory. Saf. Sci. 107, 62–76.
Nakhaee, A., Zhang, J., 2010. Trenching effects on dynamic behavior of a steel catenary riser. Ocean Eng. 37 (2–3), 277–288.
Nazir, M., Khan, F., Amyotte, P., 2008. Fatigue reliability analysis of deep water rigid marine risers associated with Morison-type wave loading. Stoch. Environ. Res. Risk Assess. 22 (3), 379–390.
Ni, Q., Ji, J., Feng, K., 2022. Data-driven prognostic scheme for bearings based on a novel health indicator and gated recurrent unit network. IEEE Trans. Ind. Inf. https://doi.org/10.1109/TII.2022.3169465.
Norske Veritas, D.E.T., 2001. Risk Assessment of Pipeline Protection.
Shen, Q., Yang, H., Zhu, Y., 2014. Reliability-based design optimization of deep-water composite catenary risers. Chin. J. Ship. Res. 9 (5), 77–84.
Smarandache, F., Dezert, J., 2013. Applications and advances of DSmT for information fusion. Instrum. Stand. Metrol. 368 (2), 417 xvi.
Tao, R., Liu, Z., Cai, R., Kang, H., 2021. A dynamic group MCDM model with intuitionistic fuzzy set: perspective of alternative queuing method. Inf. Sci. 555, 85–103.
Thorsen, M., Saevik, S., Larsen, C., 2015. Fatigue damage from time domain simulation of combined in-line and cross-flow vortex-induced vibrations. Mar. Struct. 41, 200–222.
Vatsa, M., Singh, R., Noore, A., Houck, M., 2009a. Quality-augmented fusion of level-2 and level-3 fingerprint information using DSm theory. Int. J. Approx. Reason. 50 (1), 51–61.
Vatsa, M., Singh, R., Noore, A., Houck, M., 2009b. Quality-augmented fusion of level-2 and level-3 fingerprint information using dsm theory. Int. J. Approx. Reason. 50 (1), 51–61.
Vladareanu, L., Gal, A., Yu, H., Deng, M., 2015. Improvement of the Walking Robot Dynamic Stability Using the DSmT and the Neutrosophic Logic.
Wang, K., Xue, H., Tang, W., 2013. Time domain prediction approach for cross-flow VIV induced fatigue damage of steel catenary riser near touchdown point. Appl. Ocean Res. 43 (43), 166–174.
Wang, K., Tang, W., Xue, H., 2015. Time domain approach for coupled cross-flow and in-line VIV induced fatigue damage of steel catenary riser at touchdown zone. Mar. Struct. 41, 267–287.
Xue, H., Tang, W., Qu, X., 2014. Prediction and analysis of fatigue damage due to cross-flow and in-line VIV for marine risers in non-uniform current. Ocean Eng. 83, 52–62.
Yang, D., Zhang, F., Miao, J., Zhang, H., Tao, J., 2021. Dual-rotor misalignment fault quantitative identification based on DBN and improved D-S evidence theory. Mech. Indus. 22, 24.
Yazdi, M., 2018. Risk assessment based on novel intuitionistic fuzzy-hybrid-modified TOPSIS approach. Saf. Sci. 110, 438–448.
Yi, W., Fang, Y., Jian, Z., Li, P., 2013. Dezert–Smarandache theory for multiple targets tracking in natural environment. IET Comput. Vis. 7 (6), 456–466.
Yuan, F., White, D., O'Loughlin, C., 2017. The evolution of seabed stiffness during cyclic movement in a riser touchdown zone on soft clay. Geotechnique 67 (2), 127–137.
Yuan, Y., Zheng, M., Xue, H., Tang, W., 2021. Nonlinear riser-seabed interaction response among touchdown zone of a steel catenary riser in consideration of vortex-induced vibration. Ocean Eng. 227 (3), 108891.
Zhang, W., Zhu, G., 2021. A multi-objective optimization of PCB prototyping assembly with OFA based on similarity of intuitionistic fuzzy sets. IEEE Trans. Fuzzy Syst. 29 (7), 2054–2061.
Zheng, H., Modarres-Sadeghi, Y., Dahl, J., Triantafyllou, M., 2014. Coupled inline-cross flow VIV hydrodynamic coefficients database. In: Proceedings of the International Conference on Offshore Mechanics and Arctic Engineering - OMAE, vol. 2. https://doi.org/10.1115/OMAE2014-24659.
Zhou, H., Zhao, Y., Shen, Q., Yang, L., Cai, H., 2020. Risk assessment and management via multi-source information fusion for undersea tunnel construction. Autom. ConStruct. 111 (Mar.), 103050.1-103050.16.